Experiments in Fluids (2024) 65:112
https://doi.org/10.1007/s00348-024-03841-w

RESEARCH ARTICLE

Measurements of no rotational and vibrational temperatures behind a normal shock in hypervelocity flow via absorption spectroscopy

Samuel E. Feltis[1] · Zhili Zhang[1] · Tyler S. Dean[2] · Rodney D. W. Bowersox[2] · Farhan Siddiqui[1,3] · Mark Gragston[1,3]

Received: 26 October 2023 / Revised: 17 June 2024 / Accepted: 18 June 2024 / Published online: 12 July 2024

Abstract

Tunable Diode Laser Absorption Spectroscopy (TDLAS) measurements of nitric oxide (NO) using a Quantum Cascade Laser (QCL) in the vicinity of 5.26 µm were conducted in a hypervelocity flow generated in the Texas A&M Hypervelocity Expansion Tunnel (HXT). The nascent NO was produced downstream of symmetric Mach reflections generated in Mach 8.5 flows with stagnation enthalpies from 6.9 to 11.1 MJ/kg. Path-averaged flow parameters of rotational and vibrational temperatures and NO concentration at a measurement rate of 30 kHz were obtained. By probing the R-branch of the fundamental absorption band in NO, thermal nonequilibrium and NO concentration levels in the post-shock region were measured. Measurements are compared to equilibrium calculations. NO equilibrium values during the 1 ms test period differ from the experimental rotational and vibrational measurements across the same time period. The experimental measurements of the rotational temperature show a consistent value around 3000 K larger than the recovered vibrational temperature across any run. The NO concentrations in all runs are near to the reported equilibrium value; often beginning higher than, and over time decaying to, the equilibrium concentration value of the specific tunnel run.

List of symbols

A	Einstein A-coefficient
$\widetilde{A}$	1st spin-splitting energy term
B_v	Rotational constant for vibronic level
C	2nd spin-splitting term
c	Speed of light
c_x	Constant of x broadening
c_2	2nd radiation constant
D_v	Centrifugal stretching term for the vibronic level v
d	Lorentzian–Gaussian ratio
F''	Lower-state rotational energy
f_V	Voigt convolution function
G''	Lower-state vibrational energy
g_V	Voigt convolution function
h	Planck constant
I	Moment of inertia
I_t	Transmitted signal
I_0	Baseline signal
J	Rotational quantum number
k_B	Boltzmann constant
L	Laser pathlength
M	Molecular weight
M_a	Mach number
m	Mass
N_A	Avogadro constant
n	Molecular density
n_{air}	Temperature dependence coefficient
P	Pressure
$\widetilde{P}$	Constant in the expression for Λ-doubling
Q	Molecular partition function
$\widetilde{Q}$	Constant in the expression for Λ-doubling
r_0	Molecular distance between two atoms of a diatomic molecule
S	Linestrength intensity
T_x	Temperature of x mode excitation
T_∞	Freestream temperature
t	Time
v	Vibrational quantum number

✉ Samuel E. Feltis
sfeltis@vols.utk.edu

[1] Department of Mechanical, Aerospace, and Biomedical Engineering, University of Tennessee, Knoxville, TN 37996, USA

[2] Department of Aerospace Engineering, Texas A&M University, College Station, TX 77834, USA

[3] University of Tennessee Space Institute, Tullahoma, TN 37388, USA

Y_v	Term in the ground electronic state rotational energy
α	Absorbance
α_x	Broadening due to x
γ	Heat capacity ratio
γ_x	x-broadened HWHM
$\widetilde{\gamma}$	Spin-splitting term for the excited state
ΔF	Change in rotational energy
Δf	Optical linewidth
ΔG	Change in vibrational energy
θ_x	Characteristic temperature of x mode excitation
λ	Wavelength
μ	Ratio of NO vibronic constants
ν	Wavenumber
ξ	Average noise uncertainty
σ	Absorption cross section
τ	Transmission
ϕ	Hyperfine transition term
χ	Mole fraction
ω_e	1st harmonic oscillator vibrational constant
$\omega_e x_e$	Anharmonicity constant
$\tilde{\omega}$	Term in the calculation of rotational energy

1 Introduction

Strong shockwaves are ubiquitous in hypersonic flight conditions and the increase in gas temperature through such strong compressions can result in the generation of nitric oxide (NO), the activation of vibrational energy modes of molecules, and possibly dissociation chemistry depending on the flow conditions. The molecular dissociation and redistribution of energy among the available vibrational energy modes leads to changes in the physical and transport properties of the gas that have a significant impact on the calculation of important engineering quantities such as the amount of surface heat transfer (Park 1989; Wada et al. 1993). As ground testing facilities are key to development of hypersonic flight systems, it is important to quantify these high-temperature gas effects during testing.

Tunable diode laser absorption spectroscopy (TDLAS) is a non-intrusive diagnostic technique for measuring species concentrations and obtaining information about molecular internal energy states. As an overview, every molecule and compound is able to absorb light at some wavelength and the resulting absorption spectra allow for the determination of material properties of the absorbing medium such as molecular concentration, pressure, and temperature. Often, an assumption of thermal equilibrium along the interacting pathlength of the laser with the absorbing medium is made for simplicity. However, TDLAS can be modeled to account for nonequilibrium temperatures through the use of a two-temperature model approximation; this assumes independent rotational and vibrational temperatures and states. This is important, as a common approach to modeling nonequilibrium flows in CFD is to use a multi-temperature approach where each internal energy mode (translational, rotational, vibrational, and electronic) is given a corresponding temperature. Using this two-temperature model, it is assumed that translational and rotational temperatures are identical due to similar relaxation rates, the vibrational differs due to its relatively long relaxation time, and that the electronic is negligible so long as the absorbing medium remains in the ground state. Such models and their applications in CFD are discussed in literature (Park 1989; Wada et al. 1993; Bond et al. 2021; Passiatore et al. 2022; Sweetland et al. 2018).

Thermal nonequilibrium flows stem from the varying relaxation timescales of the rotational and vibrational energy modes (Hanson et al. 2016). To wit, high energy environments may maintain, for brief periods of time, several different temperatures based on the mode of excitation. NO is a good measure of these varying excitation modes as it readily forms in hypersonic environments and contains ample variation in its absorption peaks allowing for mode differentiation (Girard et al. 2021). The use of TDLAS in hypersonic flows has been rigorously tested and shown in various experiments and literature to be a reliable measurement technique to describe such flows (Girard et al. 2021; Wehe et al. 1997; Chang et al. 2011; Schultz et al. 2014; Parker et al. 2006; Finch et al. 2020; Weisberger et al. 2016). By using TDLAS within the fundamental band R-branch of NO, the rotational and vibrational temperatures may be recovered.

In this work, nascent NO that formed behind a normal shock in a Mach 8.5 flow was analyzed via TDLAS to recover the rotational and vibrational temperatures. A two-temperature model was used to understand the effect on nonequilibrium flow behind the shockwave. Similar assumptions were also made in work by Girard et al (2021). Furthermore, all excited states are presumed to be in the $X^2\Pi$ ground state of NO, allowing for the approximation of a constant electronic partition function, removing the need to consider the electronic temperature (Hanson et al. 2016). It should be noted that the experiments were conducted in a hypersonic wind tunnel, where the inherent noise and turbulent flow are evident. The experimental TDLAS signals are raw data from the measurements, without any filtering, reflecting the reality of the conditions. This work was primarily focused on establishing a baseline analysis for TDLAS in the Texas A&M Hypervelocity Expansion Tunnel (HXT), with future interest focusing on measuring thermochemical nonequilibrium in the shear flow region of a Mach stem interaction.

2 Experimental setup

2.1 Facility and test conditions

Experiments were performed in the HXT which is described in detail by Dean et al. (2022) and depicted in Fig. 1. The 30.5 m long facility features a 0.48 m diameter pipe in the driver, driven, and expansion sections and a nozzle with a 0.92 m exit diameter is used to further expand the flow to achieve increased Mach number range, test time, and test core size. Typical facility run times are on the order of 1 ms but vary based on the target flow conditions.

The testing conditions for this work are shown in Table 1. In each test, helium was used for the driver gas; while, air was used in the driven section.

2.2 Model geometry

The model geometry used in this work is described by Dean et al (2023) and shown in Fig. 2. Measurements were carried out at approximately 30 mm behind the resulting normal shock region. The model is easily moved streamwise, which allows the TDLAS setup to remain in a fixed position during condition changes. An advantage of this geometry is its ability to generate a normal shock without a test object in the post-shock region. Similar axisymmetric concepts have been used by others (Zander et al. 2012), but the two-dimensional design of the model allows for better compatibility with optical diagnostics. The normal shock is well illustrated in Fig. 2.

The origin of the system is defined in Fig. 2a as the top of the bottom wedge. As stated previously, measurements were done in the post-normal shock region. Equilibrium conditions of the flow in this region are shown in Table 2. These calculations were done assuming a 7-species model using the JANAF thermochemical data (Chase 1998).

2.3 Tunable diode laser absorption spectroscopy setup

A schematic showing the beam path of the diode laser beam is shown in Fig. 3. The diode laser (LD-PD DFB-QCL) emission is centered around 5.26 µm with a nominal tuning capability of 30 nm depending on modulation parameters. The spectral width of the laser is below 1 MHz. The 5.26 µm beam was guided into the tunnel using a silver mirror and then turned onto a detector using another silver mirror. A bandpass filter (Thorlabs FB5250-500) was placed in front of the detector to reduce any potential contributions from other light sources. The laser current was modulated at 30 kHz to perform the necessary wavelength sweeping on a timescale comparable to the facility run time. The 30 kHz modulation and nominal facility run time of 1 ms provides around 30 cycles during the steady state.

3 Ro-vibrational model

A ro-vibrational temperature (RVT) model was created to better understand how the absorbance spectrum of NO changes in both rotational and vibrational temperature. The translational temperature is assumed to be equal to

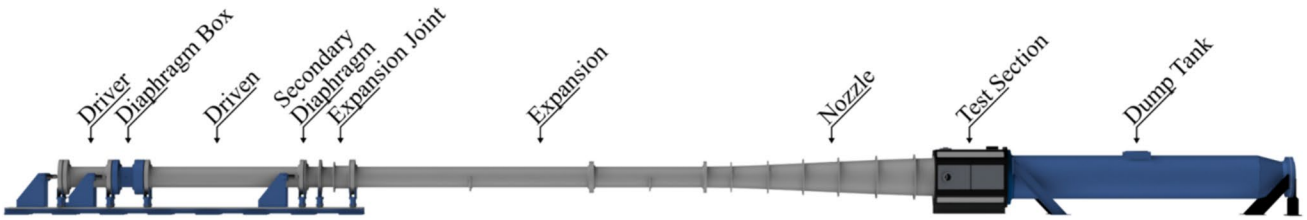

Fig. 1 The components of the Texas A&M HXT facility (Dean et al. 2022)

Table 1 Initial gas pressures and resulting flow conditions in the HXT for the TDLAS measurements

HXT run number	Driver pressure [MPa]	Driven pressure [kPa]	Expansion pressure [pa]	Mach	h_0[MJ/kg]	T_∞[K]	ρ_∞[kg/m^3]	U_∞[m/s]
219	9.65	7.24	28.93	8.6	6.9	440	0.0091	3616
220	9.31	0.59	2.67	8.5	11.1	700	0.00083	4508
221	8.34	1.93	8.80	8.5	8.8	570	0.0027	4068
222	8.34	1.93	8.80	8.5	8.8	570	0.0027	4068

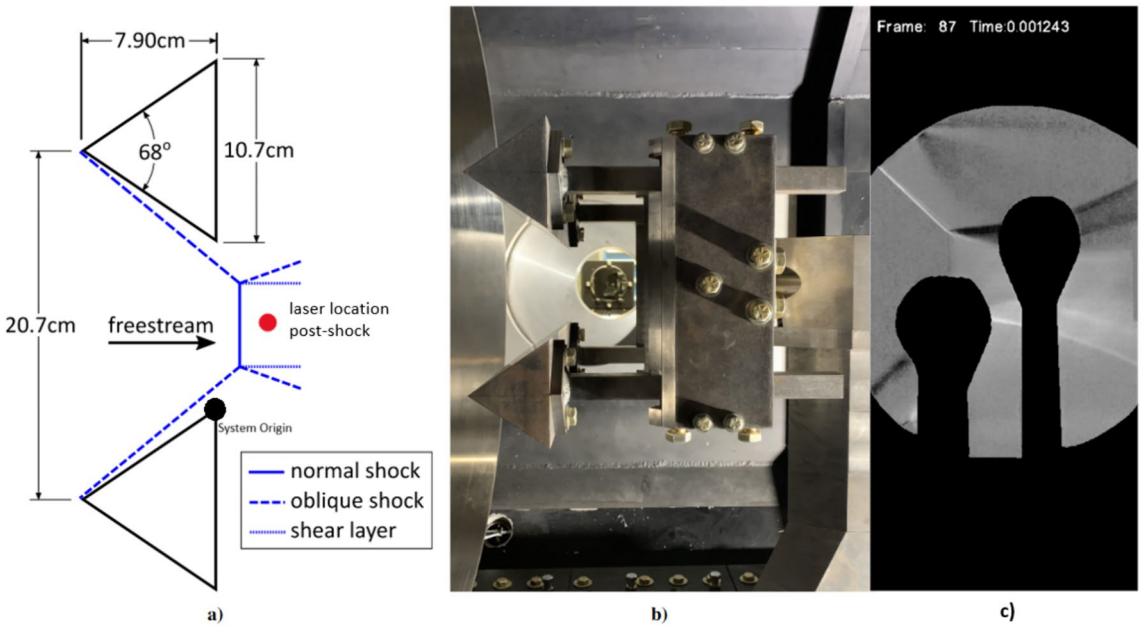

Fig. 2 **a** Dimensioned drawing of the Mach stem generator with representative flow structures and laser location, **b** a photograph as installed in the HXT test section (viewed from the side), and **c** Schlieren image visualizing Mach stems in steady state from run 221 (with mirrors for NO and atomic oxygen silhouetted)

Table 2 Equilibrium conditions for the post-normal shock region

HXT Run number	E.Q. T_2 [K]	E.Q. p_2 [kPa]	E.Q. ρ_2 [kg/m^3]	E.Q. NO Mole fraction	E.Q. NO Mass fraction
219	3780	107.94	0.0888	0.049	0.057
220	4931	15.42	0.0087	0.008	0.010
221	4285	40.85	0.0282	0.023	0.028
222	4285	40.85	0.0282	0.023	0.028

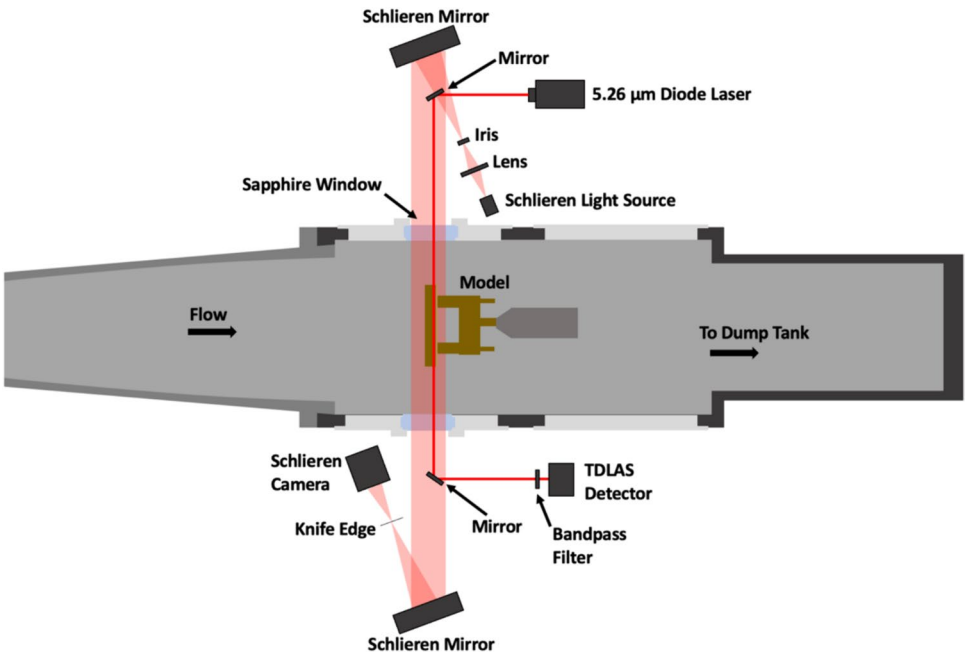

Fig. 3 A diagram showing the beam path of the diode laser beam with respect to the tunnel and model as well as the concurrent schlieren setup

that of the rotational; while, the electronic temperature component is considered negligible. This is because the transitions are all assumed to occur in the ground electronic state of NO. Beginning with the foundation of absorption spectroscopy, the Beer–Lambert Law, write,

$$\frac{I_t}{I_0} = e^{-\alpha} = \tau$$
$$\tau_i = e^{-n\sigma_i L} \tag{1}$$

where I_t is the transmitted signal through the absorbing medium and I_0 is the baseline, the signal with no absorbing species present. The ratio of these two signals relates the absorbance α to the experimental data. The transmission τ is a function of the molecular density n in cm^{-3}, the absorption cross section σ in cm^2, and the pathlength L in cm. The cross section is a function of temperature and pressure. For some transition i, σ_i is calculated via a Voigt approximation (Liu et al. 2001) as shown in Eqs. (2–4),

$$\sigma_i = \sum_j S_j(T_r, T_v) g_{V_{ij}} \tag{2}$$

$$g_{V_{ij}} = f_{V_{ij}} \frac{\nu_j}{\nu_{0,i}} \frac{\tanh\left(\frac{c_2\nu_j}{2T_r}\right)}{\tanh\left(\frac{c_2\nu_{0,i}}{2T_r}\right)} \tag{3}$$

$$f_{V_{ij}} = c_{L_i} \frac{\alpha_{V_i}}{\pi\left(\left(\nu_j - \nu_{0,i}\right)^2 + \alpha_{V_i}^2\right)} + c_{G_i}\sqrt{\frac{\ln 2}{\pi}} \frac{\exp\left(-\frac{\ln 2\left(\nu_j - \nu_{0,i}\right)^2}{\alpha_{V_i}^2}\right)}{\alpha_{V_i}} \tag{4}$$

Here, S is the line strength intensity described in Eq. (14), c_2 is the 2nd radiation constant, $\nu_{0,i}$ is the wavenumber of transition i in cm^{-1}, and ν_j is an accounting of all wavenumbers from $-\infty$ to $+\infty$ cm^{-1}; realistically this is roughly the wavenumber bounds of the laser scan range. The broadening term α_{V_i} is the Voigt broadening defined in Eq. (7). The c_L and c_G terms are the Gaussian and Lorentzian constants of the broadenings shown in Eq. (5). These terms are also found in (Liu et al. 2001).

$$c_{L_i} = 0.6818817 + 0.6129331 d_i - 0.1838439 d_i^2 - 0.1156844 d_i^3$$
$$c_{G_i} = 0.3246017 - 0.6182531 d_i + 0.1768139 d_i^2 + 0.1210944 d_i^3 \tag{5}$$

where d is a dimensionless ratio of the Lorentzian and Doppler/Gaussian broadenings,

$$d_i = \frac{\alpha_{L_i} - \alpha_{D_i}}{\alpha_{L_i} + \alpha_{D_i}} \tag{6}$$

All broadening terms are in units of cm^{-1}. The Voigt broadening is given by,

$$\alpha_{V_i} = 0.5346\alpha_{L_i} + \sqrt{0.2166\alpha_{L_i}^2 + \alpha_{D_i}^2} \tag{7}$$

The Doppler/Gaussian and Lorentzian broadening coefficients are found then in Eqs. (8–14).

$$\alpha_{D_i} = \sqrt{\alpha_{\text{laser}}^2 + \alpha_{\text{thermal},i}^2} \tag{8}$$

Thermal broadening, given in Eq. (9), is the standard Doppler broadening uninfluenced by the laser broadening. It is presumed to depend solely on the translational temperature, here assumed equal to the rotational. The laser broadening is a product of the laser itself and is often negligible due to the small size. Regardless, the recovery is shown in Eq. (10).

$$\alpha_{\text{thermal},i} = \frac{\nu_{0,i}}{c}\sqrt{\frac{2N_A k_B T_r \ln 2}{M_i}} \tag{9}$$

$$\alpha_{\text{laser}} = \frac{\Delta f}{c - \Delta f \lambda} \tag{10}$$

Here the optical linewidth Δf is given in Hz, the wavelength λ is in cm, and the speed of light c is in units of cm/s. The optical linewidth and the wavelength are properties of the laser itself and are known. The molecular weight M_i is in g/mol and is the most prominent isotopologue at the transition i centered at $\nu_{0,i}$; the constants N_A and k_b are the Avogadro and the Boltzmann constants, respectively.

Accounting for the Lorentzian broadening next, it is listed in Eq. (11) as the sum of the pressure broadening and the natural broadening. The pressure or collisional broadening will depend on the concentration of NO, the total pressure of the gas, and the rotational temperature as shown in Eq. (13). The natural broadening is a consequence of the Einstein A-coefficient seen in Eq. (12).

$$\alpha_{L_i} = \alpha_{\text{Pressure},i} + \alpha_{\text{natural},i} \tag{11}$$

$$\alpha_{\text{natural},i} = \frac{A_i}{2\pi c} \tag{12}$$

where the Einstein-A coefficient A_i is tabulated in the HITRAN database (Gordon et al. 2022) for measured lines of NO in terms of s^{-1}.

$$\alpha_{\text{Pressure},i} = \left[(1-\chi)\gamma_{\text{air},i} + \chi\gamma_{\text{self},i}\right] P\left(\frac{T_0}{T_r}\right)^{n_{\text{air},i}} \tag{13}$$

In Eq. (13) the γ_{air} and γ_{self} are the air-broadened and self-broadened HWHM per transition i given in cm^{-1}/atm in the HITRAN database alongside the temperature dependence coefficient $n_{\text{air},i}$. This broadening uses P in atm and T_r in K.

With the broadenings accounted for, to recover the absorption cross section, the line strength intensity is required. This is given by Eq. (14), modified from HITRAN for the separation of assumed equilibrium temperature into rotational and vibrational components. The units of the line strength intensity S are given in $\mathrm{cm}^{-1}/(\mathrm{molecule}\cdot\mathrm{cm}^{-2})$. A note may be made that if $T_r = T_v$ in Eq. (14) the equation used on the HITRAN website is recovered.

$$S_i(T_r,T_v) = S_i(T_0)\frac{Q(T_0,T_0)}{Q(T_r,T_v)} \exp\left[-c_2\left(\frac{F_i''}{T_r}+\frac{G_i''}{T_v}-\frac{F_i''+G_i''}{T_0}\right)\right]\frac{1-\exp\left[-c_2\left(\frac{\Delta F_i}{T_r}+\frac{\Delta G_i}{T_v}\right)\right]}{1-\exp\left[-\frac{c_2(\Delta F_i+\Delta G_i)}{T_0}\right]} \tag{14}$$

where the partition function Q is calculated in Eq. (15) taken from Hanson (Hanson, Spearrin, and Goldenstein 2016).

$$Q(T_r,T_v) = Q_{\mathrm{elec}}Q_{\mathrm{vib}}Q_{\mathrm{rot}} = (4)\left(\frac{3}{1-\exp\left(-\frac{\theta_v}{T_v}\right)}\right)\left(\frac{T_r}{\theta_r}\right) \tag{15}$$

where θ_v and θ_r are the vibrational and rotational characteristic temperatures in K, respectively. The '3' in the vibrational partition function comes from the HITRAN database and the statistical degeneracy of the most abundant isotopical vibrational band. The value of the electronic partition function comes from Eq. (16).

$$Q_{\mathrm{elec}} = (2S+1)\left(2+\delta_{0,\Lambda}\right) \tag{16}$$

The value of $\delta_{0,\Lambda}$ depends on the quantum number Λ as described in reference (Hanson et al. 2016). The $\delta_{0,\Lambda}$ value for ground state NO is zero while the value for $2S+1$ for the $X^2\Pi$ transition of NO is 2. The recovery of the characteristic temperatures of the vibrational and rotational modes are, respectively, shown in Eq. (17).

$$\theta_v = c_2\omega_e; \quad \theta_r = \frac{h^2}{8\pi^2 I k_B} \tag{17}$$

$$I = \frac{m_1 m_2}{m_1+m_2}r_0^2 \tag{18}$$

where ω_e is the 1st harmonic oscillator vibrational constant of NO and m_1 and m_2 are the masses of the oxygen and nitrogen atoms in kg, r_0 is the distance between them in m, and h and k_B are the Planck and Boltzmann constants, respectively. The vibrational and rotational energies are found from the 1992 work of J. Reisel et al. (Reisel et al. 1992) summarized in Eqs. (19–25) for the lower-state energies.

$$G(v) = \omega_e(v+0.5) - \omega_e x_e(v+0.5)^2 - \frac{\omega_e}{2} + \frac{\omega_e x_e}{4} \tag{19}$$

where v is the vibrational number of the transition and $\omega_e x_e$ is the anharmonicity constant of NO. The vibrational energy G, given in cm^{-1}, is reduced by the zero-point energy with $v = 0$. This is to more closely model the HITRAN database and the energies listed there. The rotational energy is more complex in the calculation but is gone through in Eqs. (20–24).

$$F''(J'') = B_v''\left[(J''+0.5)^2-1\right] - D_v''\left[(J''+0.5)^4-(J''+0.5)^2+1\right] \mp B_v''\sqrt{|''} \tag{20}$$

The terms B_v and D_v are vibronic constants for NO documented both in Reisel's work (Reisel et al. 1992) as well as in the NIST database. In the equation, the top symbol of the $\mp$ is for the $\Omega = {}^1/_2$ state, with the bottom symbol being for the $\Omega = {}^3/_2$ state; similarly for the double-symbol in Eqs. (22, 24). The main bulk of the rotational energy calculation is shown below, with the symbol $\tilde{\omega}''$ defined in Eq. (21), the ground state rotational energy term Y_v'' in Eq. (22) and the subsequent terms for hyperfine transitions in Eqs. (23–25).

$$\tilde{\omega}'' = \frac{(Y_v''-2)^2}{4} + \left[(J''+0.5)^2-1\right]\left(1+2\mu''\left[2(J''+0.5)^2-Y_v''\right]+\mu''^2\left\{\left[2(J''+0.5)^2-1\right]^2-1\right\}\right) \tag{21}$$

$$Y_v'' = \frac{\tilde{A}\pm C(J''-0.5)^2}{B_v''} \tag{22}$$

$$\mu'' = \frac{D_v''}{B_v''} \tag{23}$$

$$\phi(J,Y_v,\tilde{\omega}) = 0.5(J+0.5)\left\{\left[\frac{2-Y_v}{2\sqrt{\tilde{\omega}}}\mp 1\right]\left[\frac{\tilde{P}}{2}+\tilde{Q}\right]+\frac{\tilde{Q}}{\sqrt{\tilde{\omega}}}\left[(J+0.5)^2-1\right]\right\} \tag{24}$$

$$F_{\Omega e} = F_\Omega - \phi \qquad F_{\Omega f} = F_\Omega + \phi \tag{25}$$

where e and f represent the positive and negative parity recorded from the HITRAN/HITEMP databases. The values of the constants mentioned in the equations above and below are all tabulated in Reisel's work (Reisel et al. 1992). The upper-state vibrational energy is calculated in the same means as Eq. (19) only using v'' in lieu of v'' alongside the corresponding constants; the upper-state rotational energy is found with Eq. (26):

$$
\begin{aligned}
F'_{\Omega=\frac{1}{2}}(J') &= B'_v(J'+0.5)(J'-0.5) - D'_v(J'+0.5)^2 \\
&\quad (J'-0.5)^2 + 0.5\tilde{\gamma}(J'-0.5) \\
F'_{\Omega=\frac{3}{2}}(J') &= B'_v(J'+0.5)(J'+1.5) - D'_v(J'+0.5)^2 \\
&\quad (J'+1.5)^2 - 0.5\tilde{\gamma}(J'+1.5)
\end{aligned} \tag{26}
$$

With the parity being accounted for in the same manner as the lower-state energies, simply substituting the upper-state values where within Eqs. (21–25), the lower-state are written. Shown in Fig. 4 are the results of this model.

The two absorbance curves in Fig. 4 (from using the ro-vibrational model and the equilibrium model) show how the model responds to different temperature inputs maintaining the NO concentration and the pressure constant at 0.02 mol fraction and 0.4 atm.

Now that transmission has been modeled for both vibrational and rotational temperatures, the data may be fit to recover the two values through an iterative technique. The data are taken from an oscilloscope (sampled at 200 MHz), both the transmitted signal and the baseline, and analyzed in MATLAB using Eq. (1); the two signals are shown in Fig. 5 with the vibrational and rotational bands shown in Fig. 6. The data are broken into up-cycles and down-cycles dependent on whether they occur on the rise or the fall of the carrying sinewave. The periodic cycles were minimally averaged so as to better preserve the shape of each spectrum in time.

In Table 3, the subscript 1 in the Rotational Transitions column is for the value $\Omega = 1/2$; likewise, 2 for $\Omega = 3/2$. Each signal is analyzed independently through an iterative process with starting conditions equal to that of the equilibrium values shown in Table 2. Upon convergence of an answer, results are graphically plotted to confirm the success of the convergence.

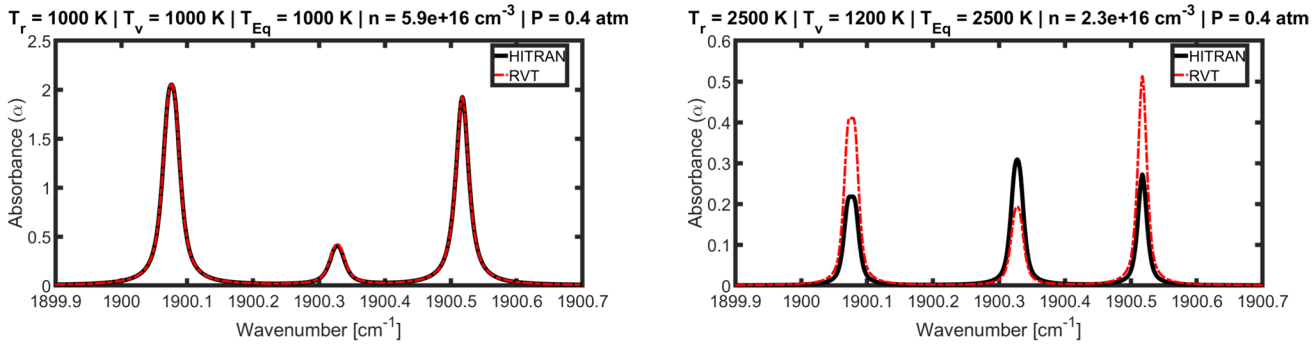

Fig. 4 Comparison of two modeled absorbance curves showing the agreement between the RVT and HITRAN (Equilibrium) models at equal temperatures and disparity at unequal temperatures

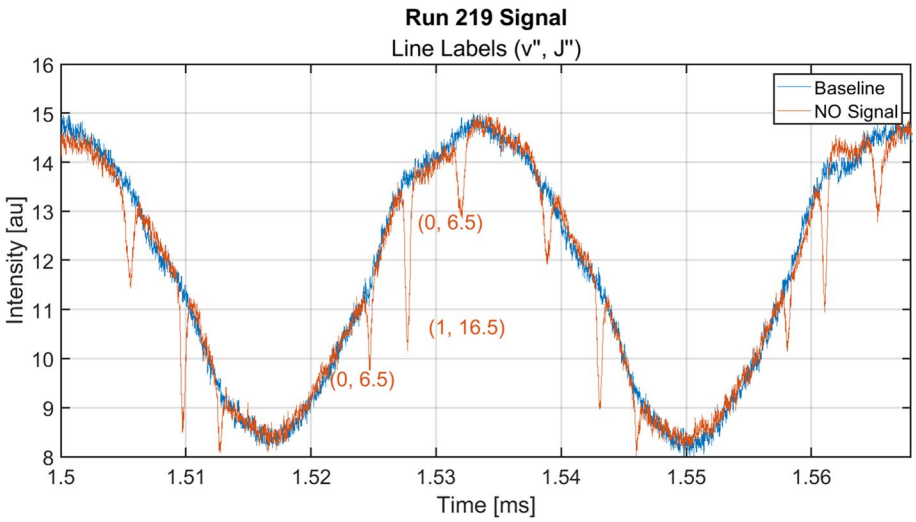

Fig. 5 Baseline signal and transmitted NO signal from Run 219

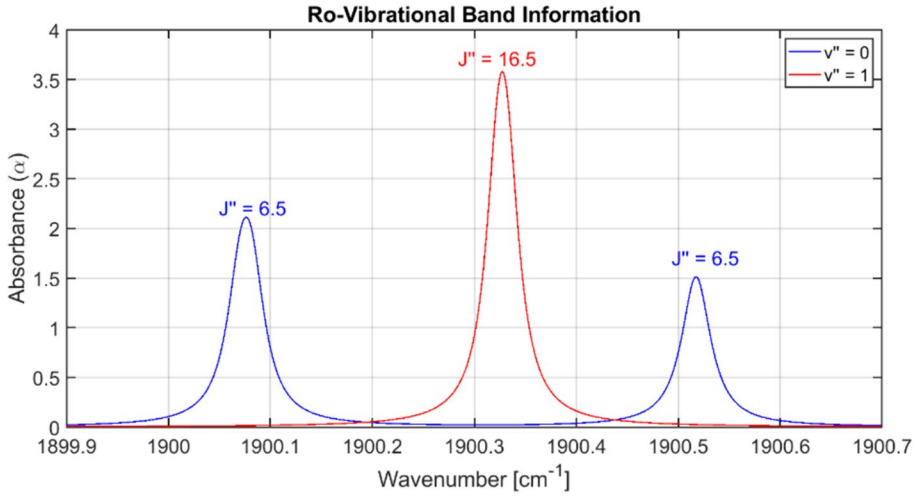

Fig. 6 Measurable bands by the QCL

Table 3 Transitional band information for the three main NO peaks

Vibrational level ($v'' \rightarrow v'$)	Rotational transitions	Extant range [cm^{-1}]
$0 \rightarrow 1$	$R_1(6.5), R_2(6.5)$	1900.071 – 1900.518
$1 \rightarrow 2$	$R_1(16.5)$	1900.324 – 1900.339

4 Data processing

To begin the data processing, the baseline spectrum is divided out from the transmitted spectrum in order to recover the transmission in accordance with Eq. (1). The baseline spectrum is taken from the early measurements of steady state of the tunnel as shown in Fig. 7. The baseline remains constant; while, the transmitted spectra are moving along the time axis.

The scans are split into up-cycles and down-cycles, and then analyzed under an equilibrium assumption to obtain initial spectral shapes. These shapes are then normalized and used as an initial guess prior to being passed through to the fitting function.

The fitting function used is a simple scan across a large range of rotational and vibrational temperatures to find a range where the residual error is within a set tolerance. When a range of minimum error is found, the sweep scans again with a smaller sweep range centered now on the prior range of minimum error.

Beginning with initial temperature guesses taken from the final equilibrium temperature of the system, a range of 5000 K centered on the equilibrium temperature is swept across for both rotational and vibrational temperatures. When a new range of minimum error is found, the center is set as the new starting point and a new sweep of just 1250 K occurs. This process repeats with each sweep comprising a smaller range of degree changes than the prior until error is below the tolerance, the temperature change would be less than 1 K, or when the temperature change oscillates between two values. This process is visualized in Fig. 8.

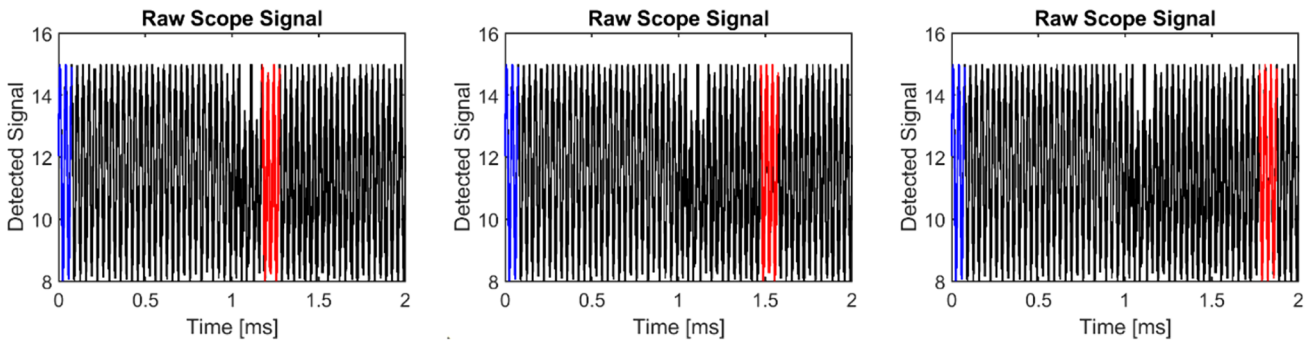

Fig. 7 Baseline spectrum is in blue and the transmitted spectrum is in red. Shown are progressive (not consecutive) selections of the transmitted spectra

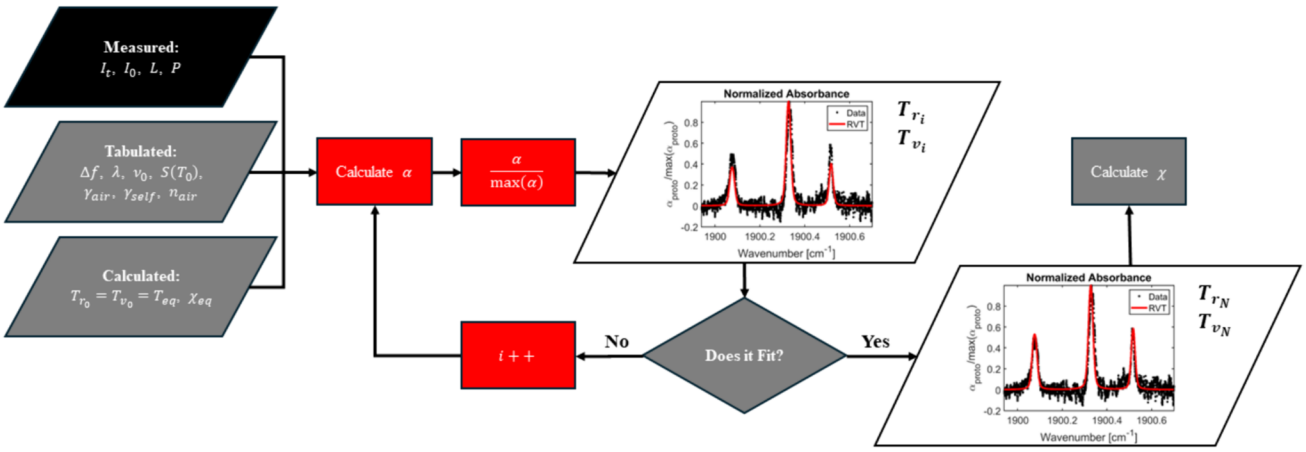

Fig. 8 Flowchart showing the operations for data processing

5 Experimental results

The four runs tested in the HXT were fitted with the above method. Most of the fits are well natured yielding minimal residual errors throughout. This is shown in Figs. 9, 10 and 11 with recovered spectra shown for illustration. Shown in black are the experimental data and in red are the RVT model fits using the equations hitherto described. Beneath each figure are the residuals for the individual spectrum.

A note will be made about run 222: an apparent sharp increase in NO concentration toward the end of steady state has been considered anomalous and has given rise to the exclusion of the run from the complete dataset. Other data points have also been disregarded. As the steady state began to decay toward the later periodic cycles, the signal to noise ratio diminished greatly as shown in Fig. 12. As such, the data just prior to the end of steady state have been discarded as correctly analyzing the rotational and vibrational temperatures from such spectra became impossible.

As the noise level reached the measured height value of the peaks, it became difficult to accurately model the temperature and the concentration of NO present in the system. This is reflected in Fig. 19 where the NO concentration tapers off toward the end of the steady state conditions.

As a fidelity check for the convergence of the temperature values, a ratio is created from the integrated absorbances of the peaks. This ratio follows the form of Eq. (27) and comes about as a means of creating a function dependent solely on the rotational and vibrational temperatures.

$$R(T_r, T_v) = \frac{A_1}{A_2} = \frac{S_1(T_r, T_v)}{S_2(T_r, T_v)} = f(T_r, T_v) \tag{27}$$

By comparing this ratio to a theoretical ideal, the temperature may be recovered for both the vibrational and the

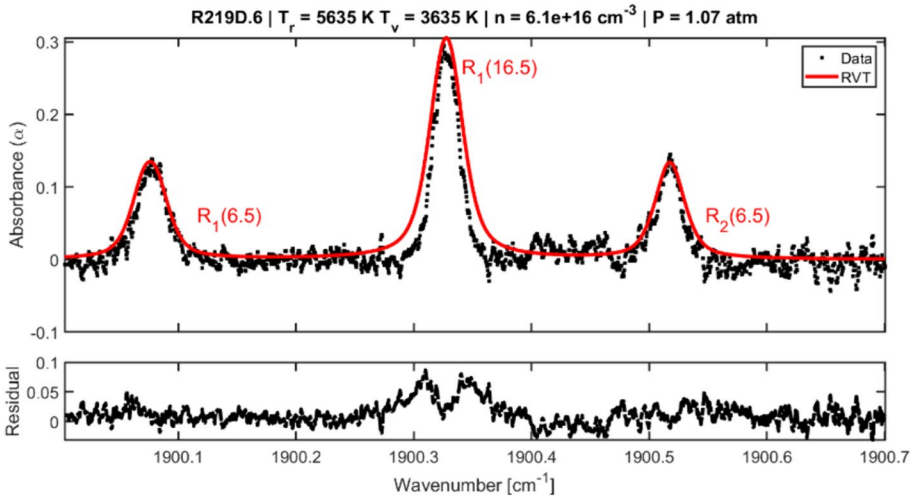

Fig. 9 Run 219, 6th down-cycle measurement

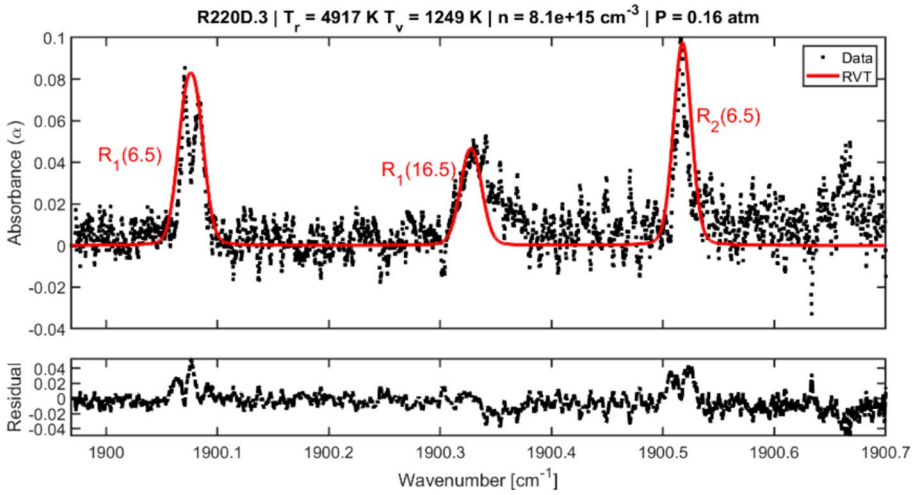

Fig. 10 Run 220, 5th down-cycle measurement

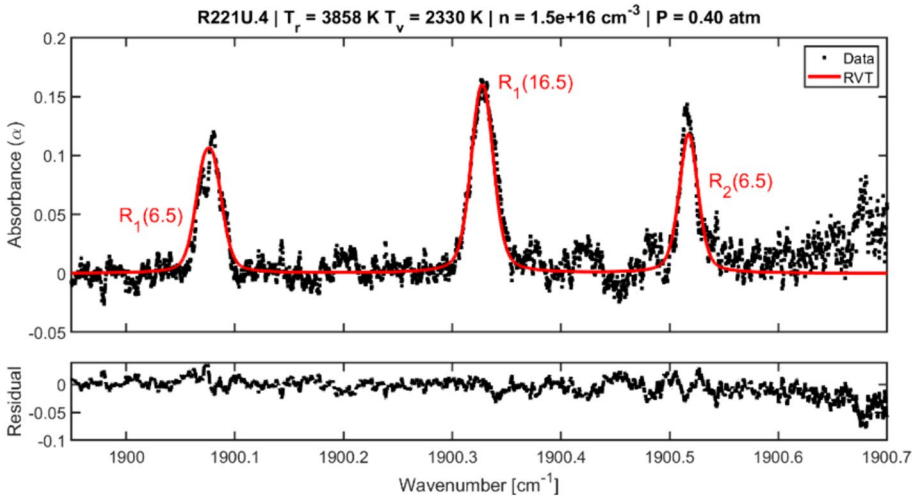

Fig. 11 Run 221, 4th up-cycle measurement

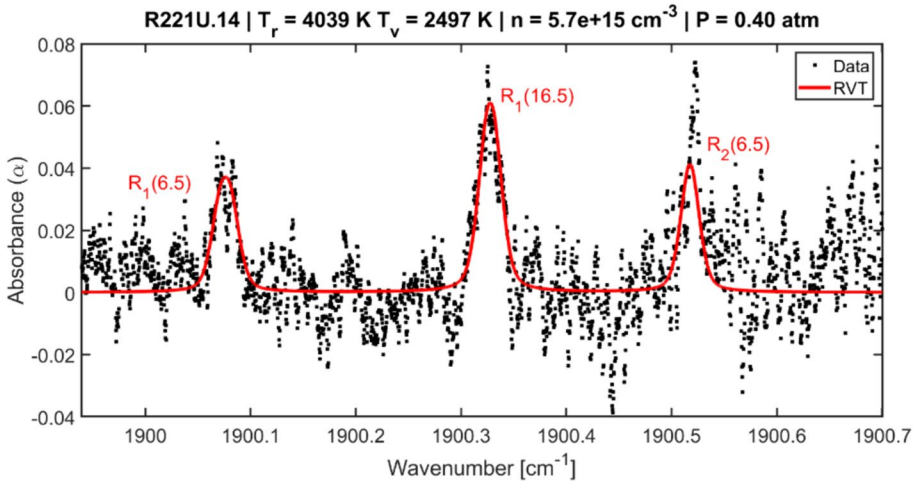

Fig. 12 Best fit for noisy, low-concentration NO data in run 221, 14th up-cycle measurement shown here as an illustration of data that were discarded

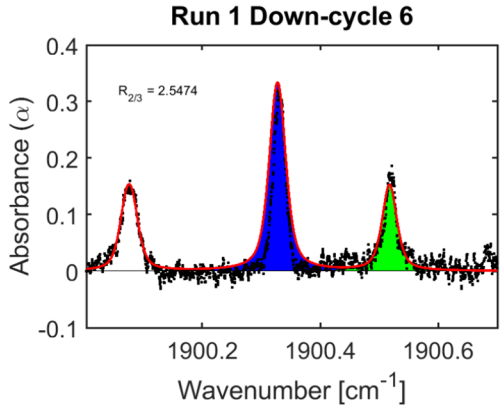

Fig. 13 Highlighted peaks for integration resulting in a ratio purely as a function of temperature

rotational values. This is shown in Figs. 13 and 14 by taking a ratio of the 2nd (middle) peak over the 3rd (right) peak.

For every temperature combination there is a unique value of R allowing for a recovery of the rotational and vibrational temperatures. The recovered temperatures match the values obtained through spectral fitting.

Figures 15, 16 and 17 show the recovered rotational and vibrational temperatures against time from the data, the trendlines of either, the calculated equilibrium temperature taken from Table 2, and the frozen temperatures for three of the four runs. As has been noted, the temperature and concentration analyses of the fourth run, numbered 222, have been discarded. The uncertainty bounds are taken using Eqs. (28–29).

$$d\tau = \text{maximum}\left[\left|\frac{\tau_{\text{sim}} - \tau_{\text{exp}}}{\tau_{\text{exp}}}\right|\right] \tag{28}$$

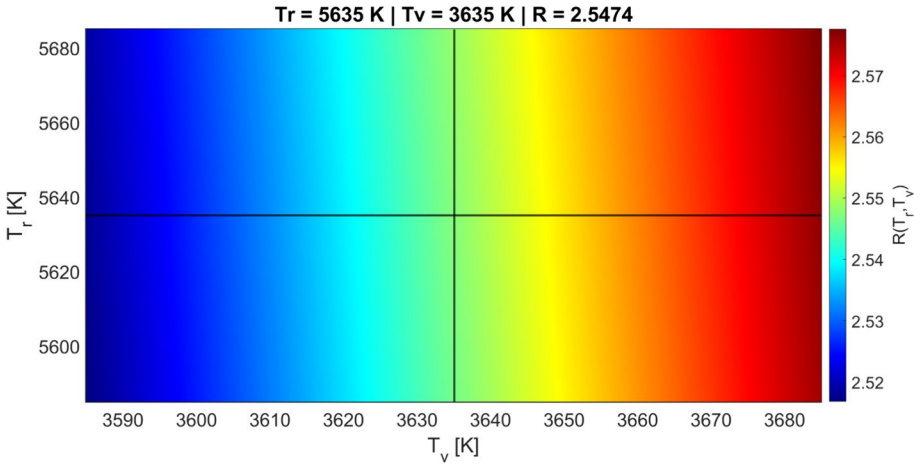

Fig. 14 $R(Tr, Tv)$ as shown in Eq. (27) and the recovered Tr and Tv values

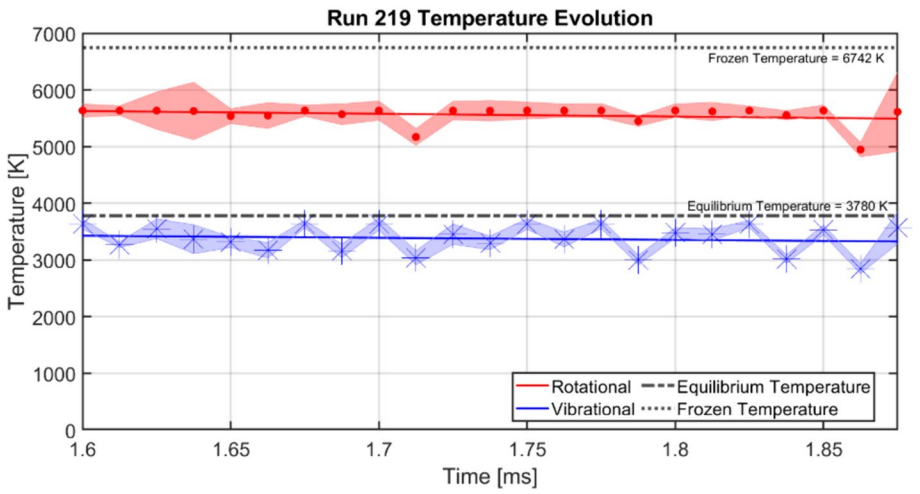

Fig. 15 Temperature evolution across run 219

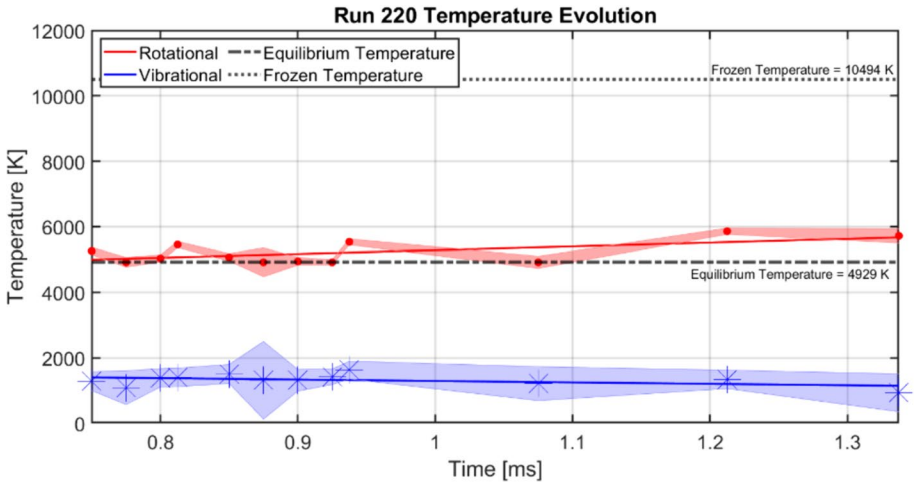

Fig. 16 Temperature evolution across run 220

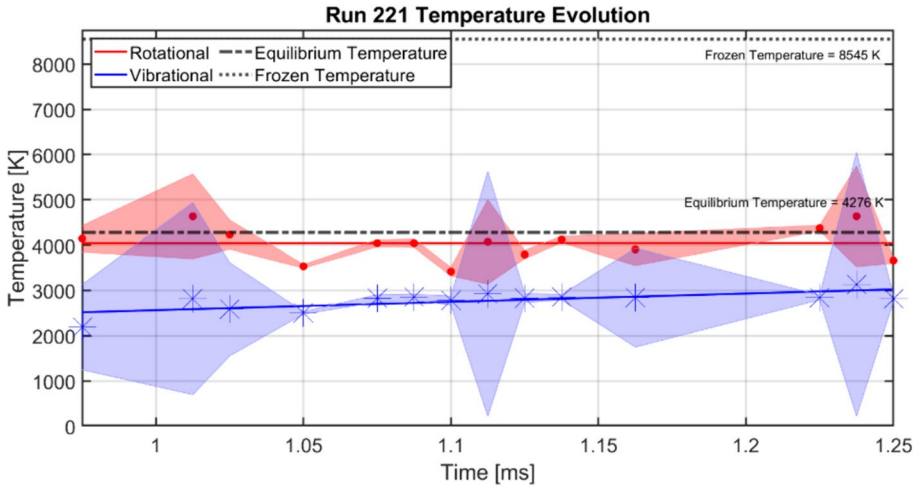

Fig. 17 Temperature evolution across run 221

$$d\tau = \frac{\partial \tau}{\partial T_r} dT_{r_0} + \frac{\partial \tau}{\partial T_v} dT_{v_0} + \frac{\partial \tau}{\partial S} dS + \frac{\partial \tau}{\partial \gamma_{\text{air}}} d\gamma_{\text{air}} + \frac{\partial \tau}{\partial \gamma_{\text{self}}} d\gamma_{\text{self}} + \frac{\partial \tau}{\partial n_{\text{air}}} dn_{\text{air}} \tag{29}$$

$$dT_r = dT_{r_0} + \xi \quad dT_v = dT_{v_0} + \xi \tag{30}$$

where τ_{sim} is the transmission of the simulated model, τ_{exp} is the transmission of the experimental data, and ξ is the average noise level in the spectrum ratioed over the spectrum maximum. The presence of ξ is to account for interfering shock structures the laser may pass through. As TDLAS is a path-integrated measurement, such structures are entangled in the data. The lower values of ξ however indicate these structures minimally interfere with the overall measurement.

To recover the maximum uncertainties for the rotational temperatures, $d\tau$ is calculated from Eq. (28) and dT_{v0} is set to zero; the value of dT_{r0} is then calculated from Eq. (29). Uncertainties for HITRAN values are tabulated in the HITRAN database. The calculated value is added onto the uncertainty from the SNR ξ and the final uncertainty of the rotational temperature dT_r is recovered. A similar process is performed for dT_v. The transmissions are found in the manner shown in Eq. (1) as just the exponential of the negative absorbance α; the partial derivatives are numerically solved. Transmission is considered in place of absorbance to remove any division by zero.

The error bounds on either side of the datapoints then are the resultant answers for dT_r and dT_v which result in the definition of $d\tau$ in Eq. (28). Any datapoints with an error bound beyond the frozen temperature or below 0 K have been discarded.

With all three analyzed runs, the rotational and vibrational temperature are plotted with an associated trendline. This trendline remains constant for the duration of steady state, indicating that the NO remains in thermal nonequilibrium for this time. To note as well, throughout any given run there would be occasional disturbances or fluctuations in the post-shock region as illustrated by the opaqueness of the

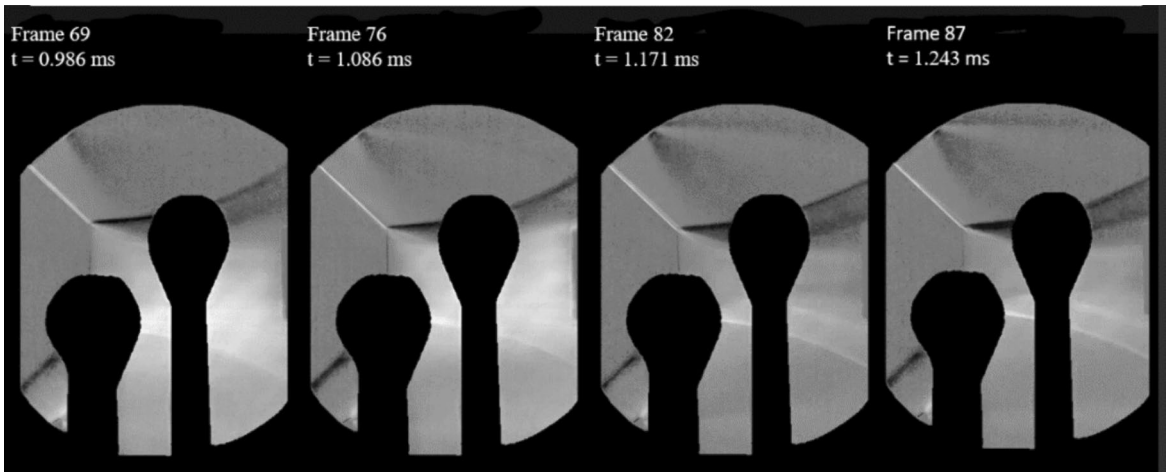

Fig. 18 Schlieren images throughout steady state of run 221 from 0.986 to 1.243 ms with beam-posts for NO and atomic oxygen detection silhouetted

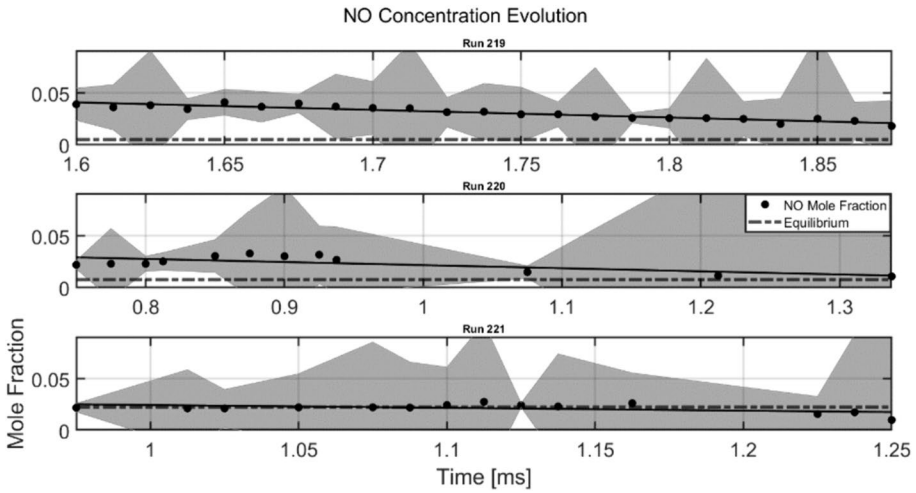

Fig. 19 Concentration changes for NO across steady state for three of the runs of the HXT

Table 4 Recovered frozen temperatures for each analyzed run

Run	Mach	Freestream temperature [K]	Frozen temperature [K]
219	8.6	440	6742
220	8.5	700	10,494
221	8.5	570	8545

flow in frames 69 and 76 of Fig. 18. Fluctuations like these are probably what causes the oscillations in the temperature and concentration data in Figs. 15, 16, 17 and 19.

The frozen temperature, the temperature assuming ideal post-shock conditions, has been calculated for all runs using Eq. (31) and the temperature data have been compared. This temperature is calculated for ideal conditions to create an upper-limit for real temperature values. For runs 220 and 221, the frozen temperature far exceeds the highest measured rotational temperature. However, in run 219, the frozen temperature is only a few hundred degrees higher than the maximum rotational temperature. This analysis is shown in Table 4.

$$T_{\text{frozen}} = \frac{\left(2\gamma M_a^2 - \gamma + 1\right)\left((\gamma - 1)M_a^2 + 2\right)}{(\gamma + 1)^2 M_a^2} T_\infty \tag{31}$$

With γ approximated to 1.4 and freestream temperature T_∞ and Mach number M_a coming from Table 1. The approximation of γ is to give an absolute maximum temperature ceiling as the practical γ will have a lower value than this, though not by a significant margin. As shown in Fig. 19 the concentration evolution across steady state follows similar

trends, with the NO concentration diminishing during the test time.

The concentration of NO is recovered by solving for n and χ in Eqs. (1) and (13) using the conversion in Eq. (32) to reduce the number of variables as the pressure is assumed known from the tests as the equilibrium pressure calculated in Table 2. The error bounds shown in Fig. 19 are the simple maximum of the absolute value of the percent error recovered from the comparison of the theoretical fits of the transmission to the experimental results in Eq. (28) added with the noise uncertainty ξ. If only the datapoints where the bounds of uncertainty remain strictly positive are considered, then Fig. 20 is recovered.

$$\chi = n\frac{k_B T_r}{P_{eq}} \tag{32}$$

The removal of concentration datapoints with error bounds that are strictly positive may be applied to the temperatures recovered in Figs. 15, 16 and 17 to further reduce possible erroneous datapoints. Performing this analysis results in Figs. 21, 22 and 23 where "reduced" indicates the poor fit concentration datapoints have been removed.

To note, for the later runs, the low concentration data had too high a noise level to be plotted in the reduced scale. Even with the reduced scale, there are still violent temperature swings in the uncertainty as highlighted in Fig. 21 where the uncertainty for at least one point exceeds 1000 K. This is not to say that the temperature is unstable at this point, rather the quality of the spectrum at that point in time leaves a large margin of error to consider. The high uncertainty bounds on the figure are there to reflect that.

To discuss whether these results hold up to scrutiny, the approximate equilibrium distances have been estimated using Table 5 and Eqs. (33–35), Landau–Teller

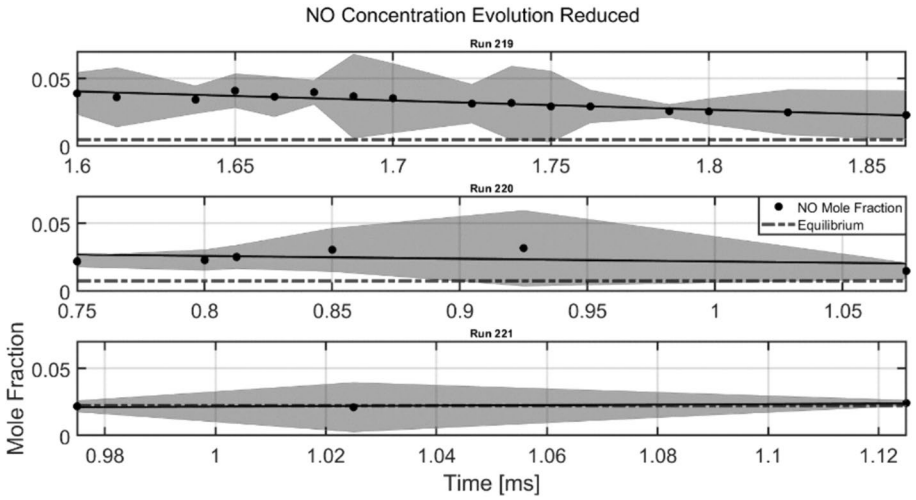

Fig. 20 Reduced NO concentration

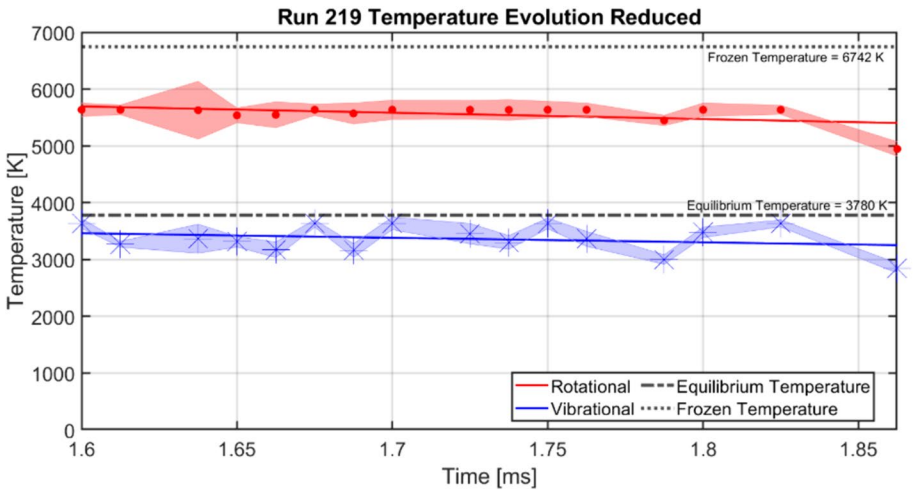

Fig. 21 Reduced run 219 rotational and vibrational temperatures

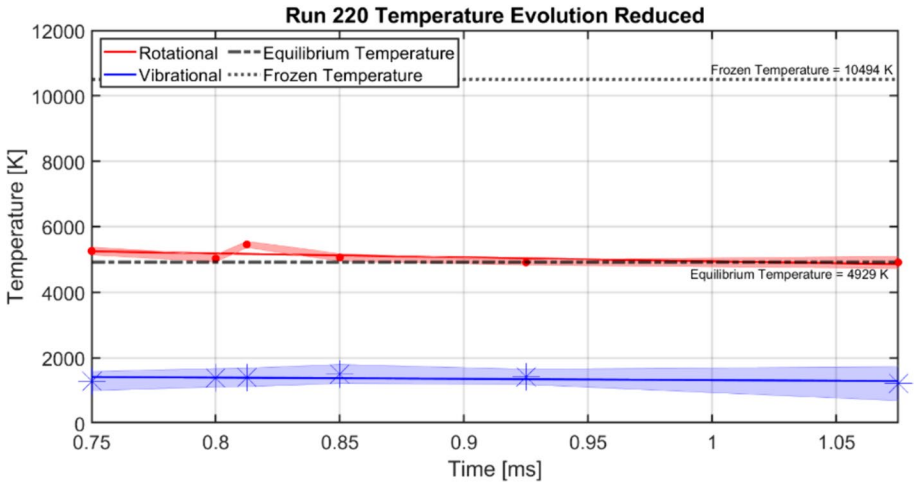

Fig. 22 Reduced run 220 rotational and vibrational temperatures

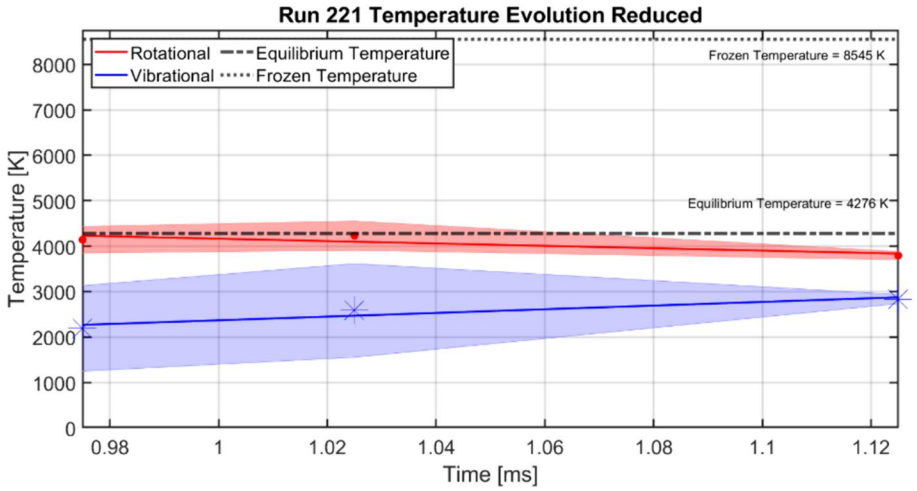

Fig. 23 Reduced run 221 rotational and vibrational temperatures

Table 5 Approximate equilibrium distances for the HXT runs

Run	Mach	P_1 [Pa]	$x_{equilibrium}+20$ [mm]
219	8.6	1149.148	22.289
220	8.5	166.747	29.005
221	8.5	441.693	24.395

The values of C_1 and C_2 for NO are 4.86×10^{-3} atm/μs and 1.37×10^{6} K, respectively

approximations, to estimate how far into the flow nonequilibrium should follow and hold.

$$P_2 = \left[\frac{2\gamma M_a^2 - \gamma + 1}{\gamma + 1}\right] P_1 \tag{33}$$

$$t = \frac{2}{P_2}\left(C_1 \exp\left[\left(\frac{C_2}{T_{\text{frozen}}}\right)^{\frac{1}{3}}\right]\right) \tag{34}$$

$$x_{\text{equilibrium}} \approx tM_a\sqrt{\gamma R T_{\text{frozen}}} \tag{35}$$

where P_1 is the freestream static pressure in Pa estimated from the driver, driven, and expansion pressures listed in Table 5 along with the NO values for C_1 and C_2. The pressure measurements are taken in the manner shown by Dean (Dean et al. 2022). From previous wind tunnel campaigns, the predicted static pressures are shown to be only 5% off measured pressures. These values then give the approximate distances the thermal nonequilibrium will bleed into the flow. The addition of the 20 mm in the total distance is to reflect that the shock forms ~ 20 mm (Bryan et al. 2023) from the back of the bottom wedge shown in Fig. 2. The NO laser was aimed directly through the tunnel at an offset

distance of 29 mm from the back of the bottom wedge, so the laser was well around the distances to measure thermal nonequilibrium for the three analyzed runs.

6 Conclusions

TDLAS, alongside an RVT model of NO, has been utilized to characterize the rotational and vibrational temperature evolution, as well as the concentration evolution of flow behind a normal shock in an expansion tunnel. From the measurable wavelengths of the IR laser, only NO was measured with negligible interference from other molecular species. These measurements were temporally resolved to provide progression data for rotational and vibrational temperature as well as NO concentration during the approximately 1 ms run time for the facility. From the data and the methodology described in this paper, it is shown that the rotational and vibrational temperatures while under steady state conditions for the HXT do not converge or decay quickly and are slightly stable around the starting conditions. Likewise, the concentration of NO in the system for the duration of steady state is consistent until the degradation of steady state begins. In total, most of the test conditions show thermal nonequilibrium between the vibrational and rotational energy states for NO behind the normal shock. Future work will seek to replicate and add on to these data for the more complete quantification of high enthalpy flows and characterization of the HXT.

Author contributions S.F. assisted in the performance of the experiment, wrote the main manuscript text, partially created figure 2 and created figures 4-16, created Tables 3-5, and created the main model used in the research analysis.Z.Z. assisted in the performance of the experiment, assisted in the creation of the model, and reviewed the manuscript.T.D. assisted in the performance of the experiment, partially created figures 2 and 3 and created figure 1, created Tables 1 and 2, and reviewed the manuscript.R.B. assisted in the performance of the experiment and reviewed the manuscript.F.S. assisted in the performance of the experiment, assisted in the creation of the model, and reviewed the manuscript.M.G. assisted in the performance of the experiment, wrote portions of the manuscript text, partially created figure 3, assisted in the creation of the model as well as the frozen temperature analysis, and reviewed the manuscript.

Funding The authors gratefully acknowledge the Office of the Under Secretary of Defense Vannevar Bush Faculty Fellowship program (Drs. B. Nair and J. Cambier, N00014-18–1-3020) for sponsoring a portion of this study. Its contents are solely the responsibility of the authors and do not necessarily represent the official views of the Department of Defense. The authors also acknowledge support from the National Science Foundation under NSF-2026242 and the DOE under DE-SC0021382.

Data availability Not applicable.

Declarations

Conflict of interest The authors declare no competing interests.

Ethical approval Not applicable.

References

Bond, Ryan B., Kenneth Tatum, Greg D. Power, and Todd Tuckey. n.d. "Capabilities of HPCMP CREATE-AV Kestrel V11 for Hypersonic flight and ground testing with a two-temperature model." In AIAA scitech 2021 forum. American institute of aeronautics and astronautics. Accessed May 24, 2023. https://doi.org/10.2514/6.2021-0236

Bryan, Caleb A., Tyler Dean, Bryan J. Morreale, and Rodney D. Bowersox (2023) "Computational simulations of hypersonic mach stems at high enthalpy." In AIAA SCITECH 2023 forum. National harbor, MD and Online: american institute of aeronautics and astronautics. https://doi.org/10.2514/6.2023-0858

Chang LS, Strand CL, Jeffries JB, Hanson RK, Diskin GS, Gaffney RL, Capriotti DP (2011) Supersonic mass-flux measurements via tunable diode laser absorption and nonuniform flow modeling. AIAA J 49(12):2783–2791. https://doi.org/10.2514/1.J051118

Chase, MW Jr. n. d. NIST-JANAF Thermochemical tables, Monograph 9. Fourth. Vol. 9. Washington DC: American chemical society. http://www.nist.gov/srd/monogr.cfm

Dean T, Blair TR, Roberts M, Limbach C, Bowersox RD n.d. "On the initial characterization of a large-scale hypervelocity expansion tunnel." In AIAA SCITECH 2022 Forum. American institute of aeronautics and astronautics. Accessed May 24, 2023. https://doi.org/10.2514/6.2022-1602.

Dean T, Blair TR, Roberts M, Limbach C, Bowersox RD (2023) "Index of refraction fluctuation spectra in aerothermochemical non-equilibrium shock layers." In AIAA SCITECH 2023 forum. AIAA SciTech Forum. American institute of aeronautics and astronautics. https://doi.org/10.2514/6.2023-0270

Finch PM, Girard J, Strand C, Yu W, Austin J, Hornung H, Hanson R n.d. "Measurements of time-resolved air freestream nitric oxide rotational, vibrational temperature and concentration in the T5 reflected shock tunnel." IN AIAA PROPULSION AND ENERGY 2020 FORUM. American institute of aeronautics and astronautics. Accessed October 6, 2023. https://doi.org/10.2514/6.2020-3714

Girard JJ, Finch PM, Strand CL, Hanson RK, Yu WM, Austin JM, Hornung HG (2021) Measurements of reflected shock tunnel freestream nitric oxide temperatures and partial pressure. AIAA J 59(12):5266–5275. https://doi.org/10.2514/1.J060596

Gordon IE, Rothman LS, Hargreaves RJ, Hashemi R, Karlovets EV, Skinner FM, Conway EK et al (2022) The HITRAN2020 Molecular spectroscopic database. J Quant Spectrosc Radiat Transfer 277:107949. https://doi.org/10.1016/j.jqsrt.2021.107949

Hanson RK, Mitchell Spearrin R, Goldenstein CS (2016) Spectroscopy and optical diagnostics for gases. Springer International Publishing, Cham. https://doi.org/10.1007/978-3-319-23252-2

Liu Y, Lin J, Huang G, Guo Y, Duan C (2001) Simple empirical analytical approximation to the voigt profile. J Opt Soc Am B 18(5):666. https://doi.org/10.1364/JOSAB.18.000666

Park C (1989) Assessment of two-temperature kinetic model for ionizing air. J Thermophys Heat Transfer 3(3):233–244. https://doi.org/10.2514/3.28771

Parker, Ronald, Thomas Wakeman, Michael Holden, and Matthew MacLean (2006) "Measuring nitric oxide freestream concentration

using quantum cascade lasers at CUBRC". In 44th AIAA Aerospace sciences meeting and exhibit. Aerospace sciences meetings. American institute of aeronautics and astronautics. https://doi.org/10.2514/6.2006-926

Passiatore D, Sciacovelli L, Cinnella P, Pascazio G (2022) Thermochemical non-equilibrium effects in turbulent hypersonic boundary layers. J Fluid Mech 941:A21. https://doi.org/10.1017/jfm.2022.283

Reisel JR, Carter CD, Laurendeau NM (1992) Einstein coefficients for rotational lines of the (0, 0) band of the NO A2Σ+−X2π System. J Quant Spectrosc Radiat Transfer 47(1):43–54. https://doi.org/10.1016/0022-4073(92)90078-I

Schultz IA, Goldenstein CS, Strand CL, Jeffries JB, Hanson RK, Goyne CP (2014) "Hypersonic scramjet testing via TDLAS measurements of temperature and column density in a reflected shock tunnel". In 52nd Aerospace sciences meeting. National harbor, Maryland: American institute of aeronautics and astronautics. https://doi.org/10.2514/6.2014-0389.

Sweetland K, Combs CS, Schmisseur JD, Rhodes R, Zhang FY, Moeller TM, Plemmons DH (2018). "Development of MIR TLAS System with Applications to Reacting Hot Gas Flows." In 2018 AIAA Aerospace sciences meeting. Kissimmee, Florida: American institute of aeronautics and astronautics. https://doi.org/10.2514/6.2018-1023

Wada Y, Ogawa S, Kubota H (1993) Thermo-chemical models for hypersonic flows. Comput Fluids 22(2):179–187. https://doi.org/10.1016/0045-7930(93)90049-F

Wehe S, Baer D, Hanson R, Wehe S, Baer D, Hanson R (1997) "Tunable diode-laser absorption measurements of temperature, velocity, and H_2O in hypervelocity flows." In 33rd Joint propulsion conference and exhibit. seattle,WA,U.S.A.: American institute of aeronautics and astronautics. https://doi.org/10.2514/6.1997-3267

Weisberger JM, DesJardin P, MacLean MG, Parker RA, Carr ZR (2016) "Near-surface CO_2 tunable diode laser absorption spectroscopy concentration measurements in the LENS-XX expansion tunnel facility." In 54th AIAA aerospace sciences meeting. San Diego, California, USA: American institute of aeronautics and astronautics. https://doi.org/10.2514/6.2016-0246

Zander F, Molder S, Morgan R, Jacobs P, Gollan R (2012) "High temperature gas effects for converging conical shocks". In 18th AIAA/3AF international space planes and hypersonic systems and technologies conference. Tours, France: American institute of aeronautics and astronautics. https://doi.org/10.2514/6.2012-5939